Original papers

Industrial scale electromagnetic grain bin monitoring

Colin Gilmore [a], Mohammad Asefi [b], Jitendra Paliwal [c], Joe LoVetri [b,*]

[a] 151 Research Inc., Winnipeg, MB R2J 1K4, Canada
[b] Department of Electrical and Computer Engineering, Room E2-390 EITC Building, University of Manitoba, 75 Chancellor's Circle, Winnipeg, MB R3T 5V6, Canada
[c] Department of Biosystems Engineering, Room E2-376 EITC Building, University of Manitoba, 75 Chancellor's Circle, Winnipeg, MB R3T 2N2, Canada

ABSTRACT

We present an Electromagnetic Imaging (EMI) system capable of detecting spoiled grain regions inside a large-scale grain storage bin. Stored grain represents significant economic and nutritional value to humankind, but despite this value, storage losses are common (estimated to vary from 2% to 30%). While there are many mechanisms that cause storage losses, virtually all of them involve higher temperature and/or moisture content of the stored grain. Increases in temperature and/or moisture both raise the complex permittivity of the grain. Our EMI system creates a 3D image of the complex permittivity through 24 antennas mounted on the side of the bin operating at a frequency of 93 MHz, combined with a 3D Finite-Element inversion/imaging code.

The antennas are designed to have both the desired electrical characteristics, as well as withstand the significant forces caused by the loading and unloading of the grain. Results with 55 tonnes of hard-red winter wheat in a ≈2500 bushel (80 tonne) bin show that our system is capable of detecting a small spoilage region (0.24% of total grain volume, 2/5 of a wavelength in size) inside dry bulk grain. The 3D EMI system is a viable method of detecting spoiled grain in industrial grain storage facilities.

© 2017 Elsevier B.V. All rights reserved.

1. Introduction

The vast majority of the world's food energy comes from a small number of staple crops which are harvested and then stored for later use. Storage times can vary from several weeks to many years. Due to the extreme importance of these crops to humanity's food supply, their safe storage is critical. Even with this importance, estimates of storage losses vary from 2% to 30% (Sinha, 1995; Muir and White, 2000), and these losses lead to economic costs estimated to be hundreds of millions of dollars in Canada alone (Jayas et al., 2011).

There are numerous threats to the quality and quantity of stored grain: the seeds may germinate while in storage, molds and fungi may grow, insect infestations may occur, or grain be eaten by rodents and other animals. For modern facilties with sealed storage bins or silos, the most important parameters of safe grain storage are the moisture content and temperature of the stored grain (FAO, 2011). High moisture content of stored grain leads to germination, mold/fungus growth, attracts insects, and also prevents the respiration of the grain (which is necessary for safe storage). Temperature is also an important parameter for safe storage of grain as low temperatures reduce the probability of early germination, as well as reducing the metabolic rates or even killing insects and molds/fungi.

Both high moisture content and high temperatures may be a cause of, and a result of spoilage. High temperatures and moisture create conditions conducive to sprouting and to mold and fungus growth; while sprouting, infestations of insects, and mold growth create heat and moisture through biochemical processes (Sinha, 1995). High temperature and moisture in stored grain is part of a positive feedback process, where high values in some spots create conditions for further spoilage, raising temperatures and moisture even further. Thus, for safe storage it is important that both moisture content and temperature be brought to, and kept at, low levels. For safe storage, these levels should also be monitored. The particular moisture/temperature level that may be considered safe depends on grain type, external conditions, and expected storage time (FAO, 2011). An example of safe storage moisture/temperatures is shown in Fig. 1. Most grains are harvested at moisture contents and temperatures that are not safe for long term storage (i.e. grain must be dried or conditioned before it may be stored safely).

Farmers and grain handlers use a variety of systems to ensure that stored grain is brought to optimal storage conditions after harvest and these conditions are maintained through the duration of
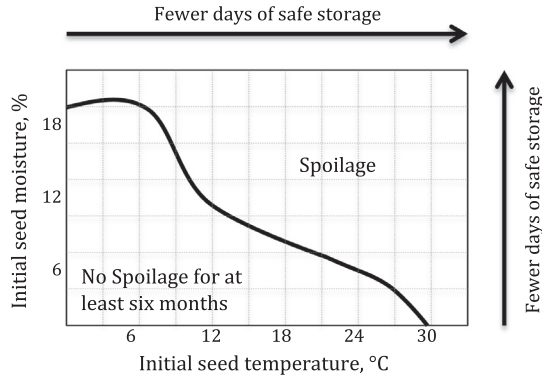
Fig. 1. An example of grain storage outcomes for wheat with varying moisture and temperatures. Modified from White (2002).
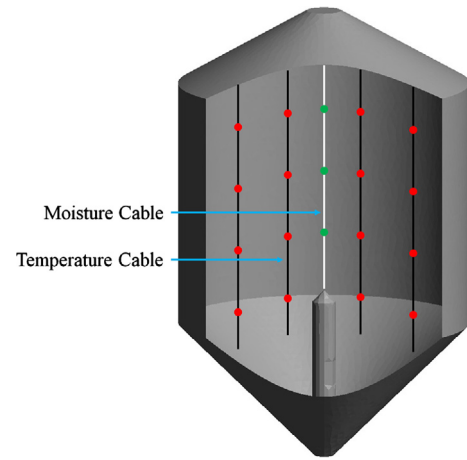

Fig. 2. A typical temperature and moisture grain monitoring system. Cables are suspended from a necessarily reinforced ceiling. Sensors are spaced approximately 1.2 m apart along each cable and are locally sensitive.

storage. These systems vary in sophistication from simply opening the top of the bin and smelling to detect moisture, mold and fungi, point sensing systems to measure moisture content of grain samples (Maier et al., 2010), temperature and moisture sensors (e.g., Folk, 2016), to chemical sensors designed to detect insect respiration products (Maier et al., 2010). Entering bins is time consuming, dangerous (Freeman et al., 1998), and not a reliable method of detecting poor storage conditions. The most common method of monitoring storage conditions is the use of a series of temperature/humidity sensors attached to cables hung from the storage bin's roof. An example of such a system is shown in Fig. 2. In such a system, point sensors measure the local temperature and humidity approximately every 1.2 m along the cable. These cable measurement systems require strengthening the roof of the bin, only sense the conditions local to each sensor, and as grain is an excellent thermal insulator, grain hot-spots (i.e. spoilage regions where the temperature has risen) can occur without detection for long periods of time (White, 2000).

In Asefi et al. (2015), we introduced the concept of monitoring the entire contents of a storage bin through the use of Electromagnetic Imaging (EMI). While many different imaging methods could be broadly construed as electromagnetic (e.g. human sight, radar, x-rays, MRI), we use EMI as a more restrictive term: by EMI, we mean the use of electromagnetic radiation to create images of materials through the use of multiple transmitting and receiving antennas, with images generated via a non-linear optimization algorithm. This is an example of an inverse scattering problem. EMI in this sense has a wide range of applications: from deep sea oil and other geophsyical prospecting (Yang et al., 2013; Abubakar et al., 2011), medical imaging (Meaney et al., 2000, 2013, 2012,, 2010, 2008), pipe-contents monitoring (Mallach et al., 2016), and more (Litman and Crocco, 2009; Joachimowicz et al., 1991; Rocca et al., 2009; Di Donato et al., 2015). Frequencies of operations vary from less than 1 Hz to the 10's of GHz range. In EMI, two simultaneous 3D images are made: one of the electrical permittivity of the contents, and another of the electrical conductivity. The permittivty relates to the speed of light in each voxel of the image, while the conductivity relates to the loss of electromagnetic energy in that voxel. These two parameters are typically combined into the complex permittivity:

$$\epsilon(\vec{r}) = \epsilon_0 \epsilon_r(\vec{r}) = \epsilon_0(\epsilon'(\vec{r}) - j\epsilon''(\vec{r})) = \epsilon_0\left(\epsilon'(\vec{r}) - j\frac{\sigma_{eff}(\vec{r})}{\omega\epsilon_0}\right) \quad (1)$$

where $\vec{r}$ is the 3D position vector, $\omega = 2\pi f$ is the angular frequency, σ_{eff} is the effective conductivity, ϵ_0 is the permittivity of free space, and $\epsilon_r = \epsilon' - j\epsilon''$ is the relative complex permittivity, henceforth referred to as the complex permittivity (or sometimes simplified to permittivity). In general, both ϵ' and σ_{eff} vary with frequency.

Electromagnetic methods of measuring grain have a long history. The fundamental reason is that grain moisture content can be inferred by measuring the bulk permittivity and conductivity, as well as the temperature of the grain, e.g. Nelson and Stetson (1976), Nelson (2008) and Nelson et al. (2000). Measurement systems consist of point systems (Nelson and Trabelsi, 2006), as well as flow-though systems (Kraszewski et al., 1998). It is important to note that inferring both the temperature and moisture content of grain simultaneously from knowledge of the complex permittivity may not be possible: there are multiple temperature/permittivity profiles that can give rise to the same complex permittivity (Nelson et al., 2000). However, for the purposes of safe storage, both high temperatures and high moisture content cause complex permittivity to rise (Nelson et al., 2000; Nelson, 2008), and most spoilage mechanisms cause both high temperatures and high moisture content (Nelson and Trabelsi, 2006).

Simply put, high permittivity and conductivity indicates spoilage (or unsafe storage conditions) of grain. Any system which can detect rises in either temperature or moisture (or both) is capable of detecting unsafe grain storage conditions.

1.1. Contributions

Within this work, we present an industrial-scale EMI imaging system and set of sensors that are an evolution of previous small-scale/lab-based imaging systems (Asefi et al., 2015; Asefi et al., 2016). The goal of this new system is to scale previous work to realistic industrial dimensions, develop a viable protocol for imaging the whole bin without complicated lab-based measurements, and prove that small regions of spoilage can be detected via this system. Specific contributions of this work include:

1. Presentation of the first industrially viable EMI imaging system for whole-bin imaging.
2. Detection and imaging of realistic grain spoilage spots.
3. Design of a set of vertically oriented antennas/sensors which are bolted to the bin wall, and have been carefully designed to withstand the extreme forces generated during bin loading/unloading procedures.
4. Avoiding the use of a direct measurement system to determine the initial permittivity of the stored grain. It is instead estimated from the prior information of the initial grain moisture content (which is commonly measured by farmers and grain handlers prior to storage).

2. Electromagnetic imaging and the inverse scattering problem

The general Electromagnetic Imaging problem (as we have defined it) involves generating EM radiation at a small number of frequencies, with multiple transmit and receive points. This problem is also known as the inverse scattering problem. A schematic of the EMI problem is shown in Fig. 3. For example, in the context of grain bin imaging, we have placed 24 antennas on the periphery of the bin wall. All possible transmit/receive pairs are then used, creating a matrix of 24×23 values. Next, a computational model is built of the physical imaging situation (e.g. the geometry of the bin), and then the collected data and this computational model are used with an optimization algorithm to find the scattering materials which best match the measured field data. Details of these inversion/imaging algorithms are beyond the scope of this work, but are available, e.g., in Abubakar et al. (2003), Zakaria et al. (2010), Zakaria et al. (2013), Abubakar et al. (2008), Haynes et al. (2011) and van den Berg and Kleinman (1997). In general, the goal of these algorithms is to determine the contrast:

$$\chi(\vec{r}) = \frac{\epsilon_r(\vec{r}) - \epsilon_b(\vec{r})}{\epsilon_b(\vec{r})} \tag{2}$$

where ϵ_b is the 'background' complex permittivity. There is some flexibility in selecting the definition of the background permittivity. The use of non-uniform backgrounds is discussed further in Section 4.4.

2.1. Inversion code

Herein, we use the inversion code outlined in Zakaria et al. (2013). This code uses the Finite-Element-Method (FEM), and computes the 3D vectorial electric field:

$$\nabla \times \nabla \times \vec{E}^{sct} - k_b^2(\vec{r})\vec{E}^{sct}(\vec{r}) = k_b^2 \vec{w}(\vec{r}) \tag{3}$$

where $\vec{r}$ is the 3D position vector, $\vec{E}^{sct}(\vec{r})$ are the scattered fields caused by presence of the scattering objects, $k_b^2 = 2\pi f \sqrt{\mu_0 \epsilon_0 \epsilon_b(\vec{r})}$ is the (spatially varying) background wave-number, and $\vec{w}$ are the contrast sources:

$$\vec{w}(\vec{r}) \triangleq \chi(\vec{r})\vec{E}^{tot}(\vec{r}) \tag{4}$$

and $\vec{E}^{tot}(\vec{r}) = \vec{E}^{inc}(\vec{r}) + \vec{E}^{sct}(\vec{r})$ are the total fields. The inversion code works by minimizing the following equation:

$$F(\chi, \vec{w}) = F^S(\vec{w}) + F^D(\chi, \vec{w})$$
$$= \frac{\left\| \vec{E}_{meas}^{sct} - \mathcal{G}_S\{\vec{w}\} \right\|_S^2}{\left\| \vec{E}_{meas}^{sct} \right\|_S^2} + \frac{\left\| \chi\vec{E}^{inc} - \vec{w} + \chi\mathcal{G}_D\{\vec{w}\} \right\|_D^2}{\left\| \chi\vec{E}^{inc} \right\|_D^2} \tag{5}$$

where $\mathcal{G}_S$ is the field operator that takes the incident field and contrast and generates the scattered fields, and $\mathcal{G}_D$ is the field operator that takes in the incident field and contrast and generates the total fields inside the imaging region. $F^S(\vec{w})$ is called the data error, and measures the difference between the simulated and measured scattered fields, and $F^D(\chi, \vec{w})$ is called the domain error, which measures the field errors between the total fields inside the imaging domain. Details of the inversion process may be found in Zakaria et al. (2013). When desired (e.g. at antenna locations), the magnetic fields $H(\vec{r})$ are calculated with Faraday's law, as described in Asefi et al. (2016).

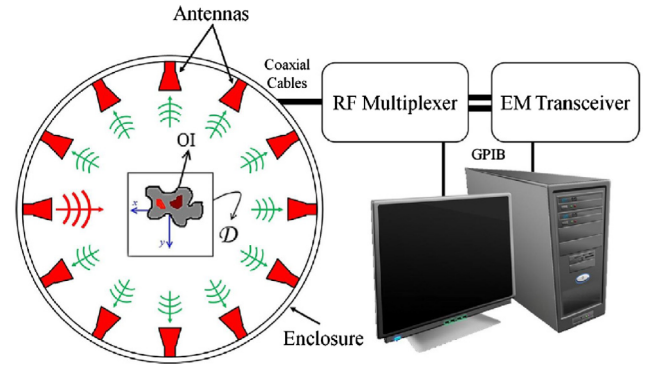**Fig. 3.** Example of an EMI system.

3. Field probe/antenna design

The EMI process relies on (a) producing a known interrogation field inside the measurement region, and (b) accurately measuring that field. Both of these processes require antennas/field probes inside the bin. There is an engineering trade-off in the sensor design: the ideal transmitter will efficiently transmit a known field pattern into the bin, while the receivers will measure this field at a single point without perturbing this field. However, as the transmitters and receivers are the same antennas in our system, the ability to efficiently transmit a field in the bin is at odds with the ability to detect a small-region local field without perturbation. This trade-off is a consequence of reciprocity, and means no antenna/field probe will have all the desired characteristics. Within this work, we have chosen to use sensors which are closer to field probes, in that they are very inefficient at transmitting energy into the imaging region, but accurately measure fields at a point. As such, we will refer to our sensors as field probes throughout.

3.1. Electrical design

Many EMI systems rely on measuring the E_z field surrounding the target, e.g., Meaney et al. (2000), Gilmore et al. (2010) and Belkebir and Saillard (2005). However, within a metallic chamber, the tangential component of the electric field (E_z), as well as the normal component of the magnetic field, vanish close to an electrical conducting wall. To accomdate for this, we previously developed a system with normal-electric field component measurementusingd monopole antennas placed normal to the chamber/bin walls (Asefi et al., 2016; Asefi et al., 2017). However, these monopole antennas can not be used inside of an industrial grain bin: they must be sized approximately 1/4 of a wavelength, which for our test 2500 bushel bin means they protrude approximately 1 m into the interior.[1] Even with slow (approx. hour long) loading and unloading processes, these antennas are unable to withstand the unloading forces. Further, their large size compared to wavelength means that they create an undesired large perturbation of the fields inside the bin.

To avoid the mechanical problems, yet maintain the desired electrical properties, a shielded half-loop (surface current measurement) field probe was developed in Asefi et al. (2016). Since we have designed our probes to remain close to the metallic bin wall, the dominant field components are the normal component of the electric field and the tangential components of the magnetic field. Because the field probe outputs a single voltage corresponding to the total field at its location, a simple wire loop (without a shield) cannot distinguish between the remaining field compo-

---

[1] We have tested antennas of this type in an industrial grain bin.

nents (normal *E* and tangential *H*), and the voltage at the terminal remains a combination of these two components. It is our design goal to only measure the tangential magnetic field in the bin. Thus, we must find a way to remove the effects of the normal E field. With our wire loop design, it is the parts of the wire normal to the bin wall that pick up the normal component of the electric field. To eliminate the contribution of the normal E-field to the voltage, we use shielded coaxial cables, with a small cut (approx. 1 mm) on the long axis of the probe. This significantly reduces the electric field coupling to the probe arms normal to the bin wall, and the voltage measured by the probe will be primarily due to the tangential magnetic field passing through the cable loop. The principles of this field probe type can be found in Dyson (1973), Kanda (1993) and Spiegel et al. (1983). An electric model of our probe is shown in Fig. 4. This probe measures the tangential magnetic field passing through the loop, and produces a voltage

$$V_e = -j\omega\mu HA \qquad (6)$$

where *H* is the magnetic field tangential to the loop, *A* is the area of the loop, μ is the permiability, and ω is the radial frequency.

For our probe, the shielded half loop is 40.64 cm long and stands 10 cm off the bin wall. At our operating frequency of 93 MHz, the length of the antennas is approximately 1/4 of a wavelength (with the wavelength measured in dry grain). For these field probes, the transmit/receive cable is attached to the top connector. The bottom connector is grounded with a grounding connector.

3.2. Mechanical design

In addition to having the required electrical characteristics, field probes in an industrial grain bin must withstand the forces caused by the unloading and loading of the bin contents. While there are a few mechanisms for generating forces on a field probe in the bin (e.g. friction), the largest forces on the probes occur during the unloading process when the field probe may need to hold up the entire column of grain above it. For example, when a grain storage bin is unloaded, air can generally flow between the grain. Since the bin is unloaded from the bottom, this means that as the grain flows out of the bin, air pockets will open up below any obstruction - and thus any grain remaining above the antenna must be held up by the field probe mounting system. The forces involved in these air pockets can be very large: as previously mentioned, bin roofs must be strengthened at construction time to support the temperature/-moisture cables, and internal ladders are commonly ripped off their mounting bolts and destroyed.

With this in mind, we designed an enclosure for the probe that is capable of withstanding these forces. Images and schematics of this field probe are shown in Fig. 5. The primary method of minimizing the forces is to place the probe vertically in bin (previous prototypes on a small lab-based system were horizontal (Asefi et al., 2016)). Further, angled edges on top and bottom spill any grain that is trapped above the probe.

For structural strength, the enclosure is constructed of two pieces of polycarbonate machined as shown in Fig. 5. Inside of the polycarbonate a machined channel to hold the coaxial cable (this cable is the electrical component of the probe, with a 1 mm cut in the outer conductor). There is also a steel grounding plate to ensure connectors are grounded, and this plate has 16 mounting holes for screws or bolts. Polycarbonate was selected as the enclosure material for its structural strength and ability to be machined. The shape of the polycarbonate shield is structurally rigid, and is designed to fit into the corrugations of the bin wall.[2] Further, the

---

[2] We note that the bin used for experiments in this paper is not corrugated, but the majority of bins are. These probes can be installed on straight sided bins.
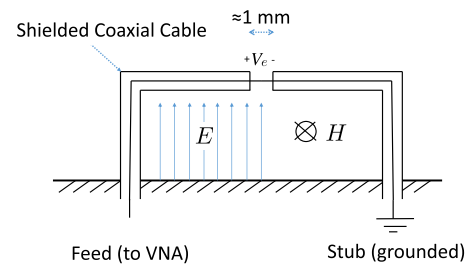

Fig. 4. Electrical model of the field probe/antenna.

(a)   (b)
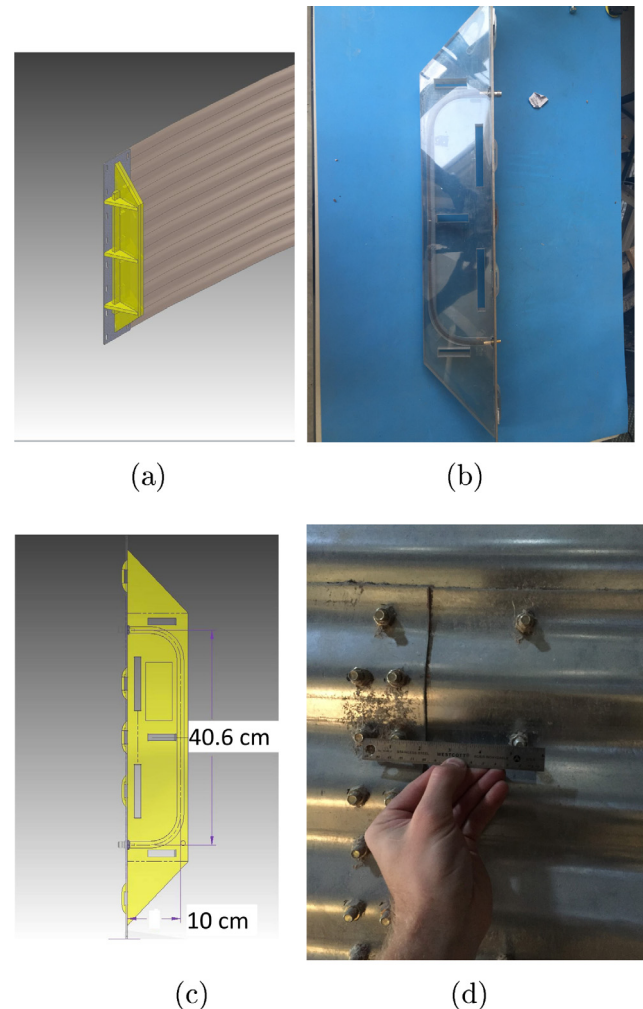

(c)   (d)

Fig. 5. Design of field probe/antenna. (a) 3D ISO image, (b) photograph of antenna, (c) side ISO image with dimensions (cm), (d) matching hole pattern on typical storage bin. The probe cable is 40.6 cm long and is held 10 cm off the bin wall.

exterior ground plate has been designed such that it will fit standard bolt-hole spacing in corrugated bins (as shown in Fig. 5(d)).

4. Experimental setup

4.1. Hardware

For data collection, we used a commercial Vector Network Analyzer (VNA) (Agilent PNA E8363) and a 2×24 port mechanical switch (Agilent 87050A-K24). Between the source port of the VNA and the switch, we placed a 20 dB amplifier (ZFL-2500VH+ (Option B): 20 dB gain). This amplifier was needed to ensure that there was enough received signal. For example, at the operating
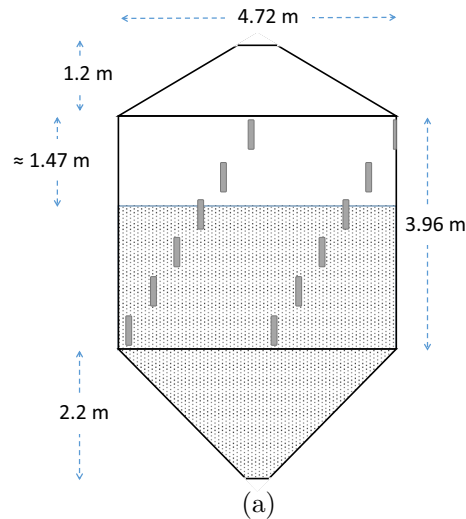
Fig. 6. (a) Approximate dimensions of the hopper bin in meters, with the approx. placement of the field probes and grain fill height shown. (b) Photograph of the interior of the bin, partially filled with hard-red-winter wheat with two exposed antennas and one partially buried antenna; and (c) photograph of the exterior of the bin.

frequency used herein (93 MHz), our antennas reflect back approximately 1/2 the energy the VNA transmits (i.e. $S_{x,x}(93 \text{ MHz}) \approx -3$ dB). The transmit power of the VNA was set to 0 dBm, for a total input power of 20 dBm.

4.2. Bin and grain

For testing, we used a hopper-style bin filled with approximately 55 tonnes of hard-red winter wheat. A diagram showing the dimensions of the bin is shown in Fig. 6. At 55 tonnes, the bin was approximately 2/3 full (the grain level can be clearly seen in our results, Figs. 9 and 11). This grain was measured to be approximately at 15% moisture content.[3] From the literature, we estimated the complex permittivity of the grain to be $3.9 - j0.38$ (Nelson and Stetson, 1976).[4]

---

[3] Moisture content is measured in % moisture by weight of the grain.

[4] For all permittivity estimates in this paper, we have used the data in Nelson and Stetson (1976) at 100 MHz (our system works at 93 MHz). The use of the 100 MHz data is justified by the minor changes in wheat permittivities around the 100 MHz frequency range: see, e.g., Lawrence et al. (1998).

The 24 field probes were attached to the bin in 6 vertical levels of 4 probes each. Each vertical level was shifted 15° from the one below, creating a spiraling pattern. This pattern is shown in Fig. 6(a).

Typically, when grain transferred to the bin, the grain pours into the bin in from a single point in the middle of the roof. This results in the a heaped conical top surface, with the angle of repose dependent on the type and moisture content of the grain. For this experiment, we require knowledge of the placement of the dry grain in the bin (see Section 4.4). With the goal of keeping our computational model as accurate as possible, we manually flattened the heaped conical surface to make it approximately horizontal.

4.3. Spoilage target

Ideally, tests of the imaging system would involve natural spoilage spots that spread organically throughout a bin. However, the large cost of the wheat in our test bin prevents us from creating uncontrolled spoilage within the bin. Thus, we have created a contained spoilage target in a thin-walled plastic container (a garbage can).
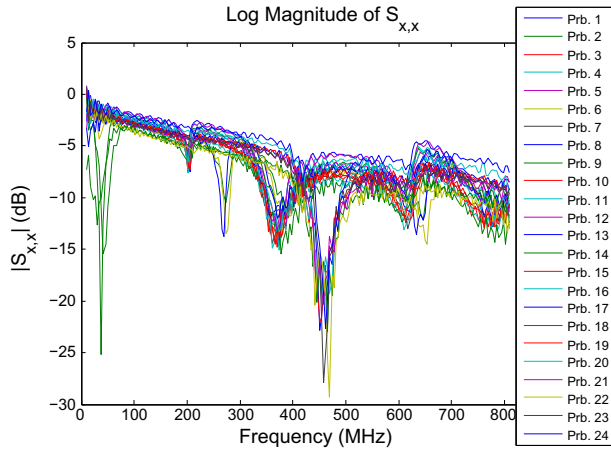
Fig. 7. $|S_{x,x}|$ of 24 installed field probes in grain bin, partially filled with grain, from 10 to 800 MHz. Differences in probe response are largely caused by location within the bin (e.g. in grain, out of grain, and partially submerged in grain).
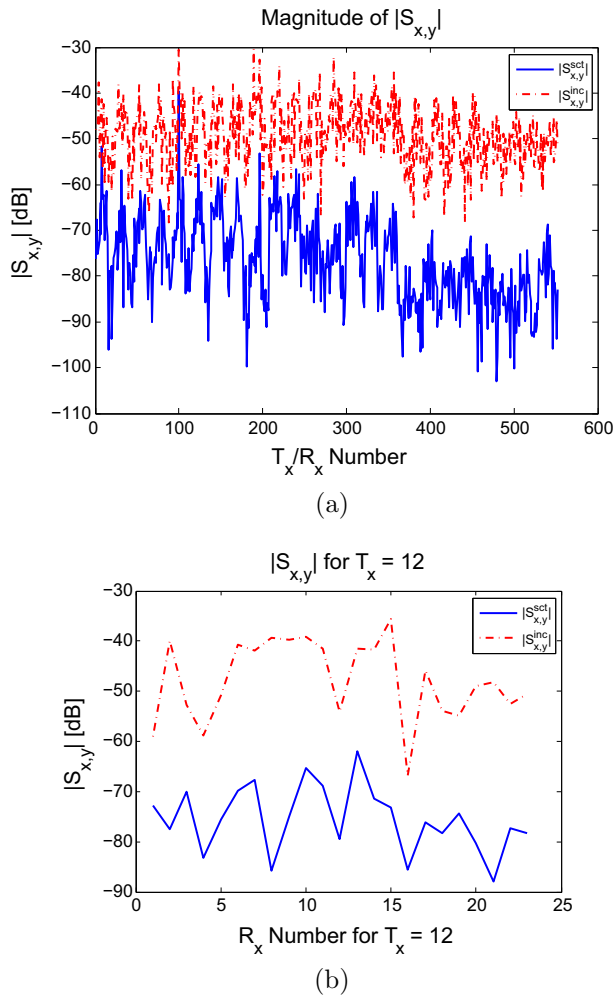

(a)

(b)

Fig. 8. (a) Magnitude of $S_{x,y}$ measurements for target position # 2, 93 MHz, for all transmit and receive pairs. Both the incident and scattered field are shown. Note that the magnitude and phase of the $S_{x,y}$ data are the entirety of data used to generate the images for target position 2 in Figs. 11 and 12 (we do not show the phase data). The scattered field measures the fields caused by the inclusion of the spoilage target. (b) Close up of $S_{x,y}$ data for transmitter number 12. Note that the scattered field measurement is well above the noise floor of the receiver system (-120 dB), despite the field probes having an $S_{x,x}$ of approximately -1.5 to -3 dB at 93 MHz.

The container is approximately 55.7 cm in diameter, 70.5 cm in height, and has a total volume of 121.1 L. This represents a spoilage region of $\approx 0.24\%$ of the total grain volume in the bin. The maximum dimension of the target is approximately $2/5$ of a wavelength of our interrogating field (when the wavelength is measured inside the dry 15% wheat). We filled the container with dry (15%) wheat, added water to the container, and stirred the grain. This container was then left for approximately 24 h in order to let the moisture be absorbed by the grain, and excess water was then drained. Total weight of the spoiled grain was approximately 85 kg. Grain moisture content was then measured with a commercial device[5] to be 25%. At this moisture content, the complex permittivity is approximately $4.9 - j0.7$ (Nelson and Stetson, 1976).[6] Imaging of the grain took place approximately 48–72 h after this spoiled grain target was created.

4.4. Inversion procedure

The fundamental goal of the inversion/imaging procedure is to obtain the contrast (Eq. (2)), which summarizes all knowledge of the materials in the bin, including both the total permittivity and background permittivity. As mentioned, however, the definition of the background permittivity is flexible. For the grain storage problem, we chose the background contrast to include the initial (dry, unspoiled) grain in the bin. To include this information in the inversion algorithm, this means we must know the location and permittivity of the initial grain used to fill the bin. The assumed knowledge about the initial permittivity of grain in the bin is acceptable because grain producers/handlers regularly measure the moisture content of grain prior to and during storage. For example, we measured the hard red winter wheat to be 15% moisture content, which has an expected permittivity of $3.9 - j0.38$ (Nelson and Stetson, 1976). The assumed knowledge of the fill level/location of the initial grain level is currently an issue as this information (while it may be estimated) is not available in an accurate form at most industrial sites. For the purposes of this work, we assume this knowledge of the grain height is available and leave determining the level to future work.[7]

The basic work-flow and data calibration method for our experiment was as follows:

1. The moisture content of the grain was measured with a commercial device. From this, the complex permittivity was estimated (from, e.g., Nelson and Stetson, 1976).
2. The grain was flattened, and its distance from the bin top measured.
3. Using the knowledge of the bin geometry and initial grain distribution, we compute the simulated incident magnetic (H) fields at the receiver locations from our FEM-based computational model for every transmitter (at the operating frequency of our system, 93 MHz). These fields are denoted H_{sim}^{inc}. This results in 24×23 values.
4. Next, with only the dry grain present in the bin, a full set of experimental data were collected (for our case, 24×23 measurement points). These data are referred to as the incident s-parameters: S_{meas}^{inc}.
5. We compute the calibration coefficients (which convert s-parameters to field values) as:

---

[5] The mini GAC plus moisture tester (Dickey-John, Auburn, IL).

[6] For the estimate of grain at 25% we have extrapolated slightly beyond the 3–23.8% moisture contents reported in Nelson and Stetson (1976).

[7] There are multiple methods that may be able to determine the initial grain level and distribution with our measurement system, but we leave this for future work.

$$C = \frac{H^{inc}_{sim}}{S^{inc}_{meas}} \tag{7}$$

These coefficients are calculated for each transmit/receive pair (there are 24×23 calibration coefficients). In addition to converting s-parameters to field values, the calibration coefficients minimize/eliminate the differences between our computational model and the experimental system.

6. The spoilage target (described in Section 4.3) was buried in the grain, with the top of the grain approximately 0.35 meters below the upper surface. A set of measurements were again taken. This process is meant to represent the organic spoilage of grain in the bin. These measurements are referred to as the total s-parameters S^{tot}_{meas}. This again results in 24×23 values.

7. The scattered s-parameters are calculated: $S^{sct} = S^{tot} - S^{inc}$. These parameters represent the changes in EM fields caused by the grain spoilage. These scattered s-parameters are converted to calibrated estimates of the fields at the receivers through the calibration coefficients generated above:

$$H^{sct}_{meas,cal} = CS^{sct} = \frac{H^{inc}_{sim}}{S^{inc}_{meas}} S^{sct}. \tag{8}$$

8. The initial physical model used in step 2, along with the calibrated scattered field data, $H^{sct}_{meas,cal}$ are then passed to the inversion code, which generates the final image.

(a) Vertical section $Re(\epsilon_r)$

(b) Horizontal section $Re(\epsilon_r)$

(c) Vertical section $-Im(\epsilon_r)$

(d) Horizontal section $-Im(\epsilon_r)$
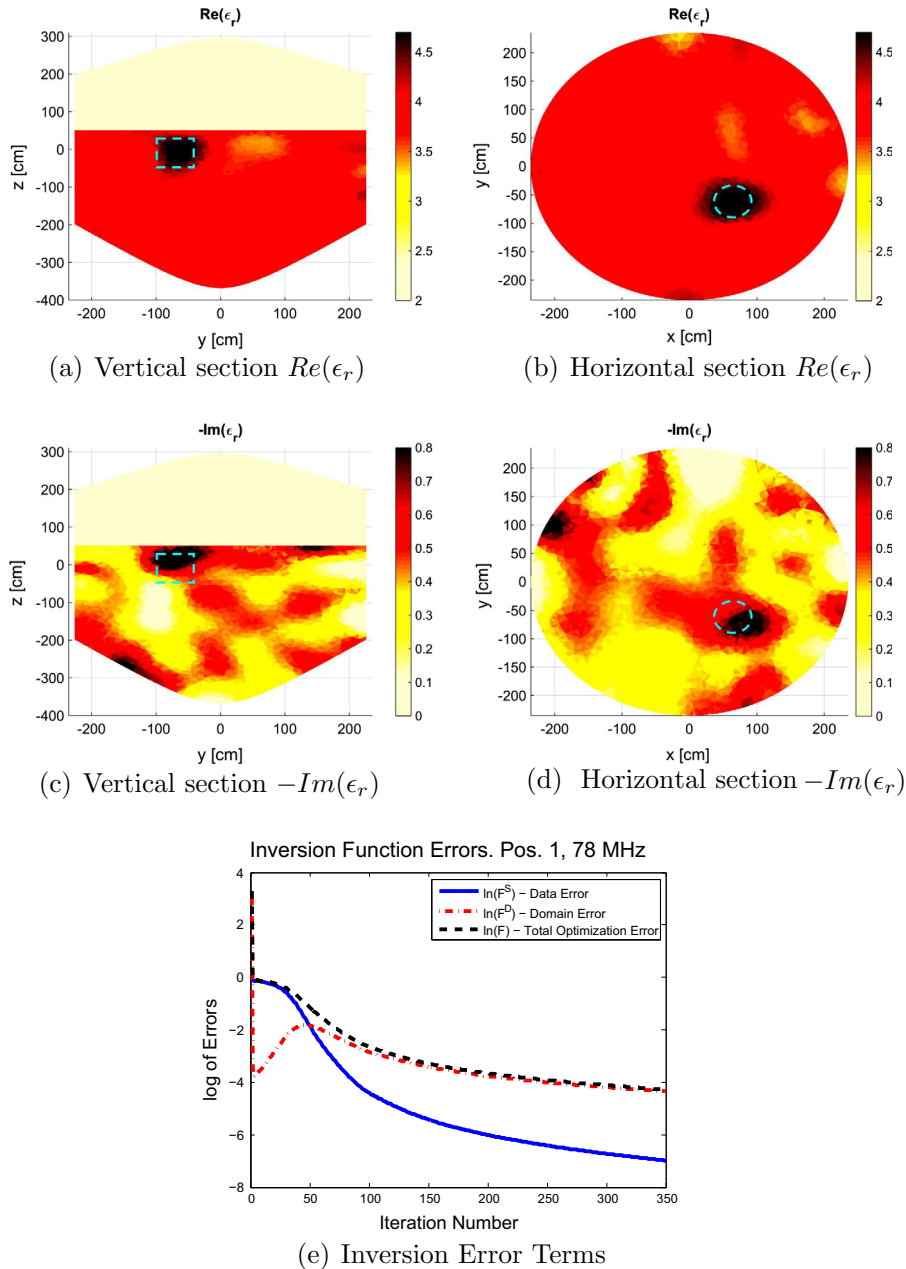
(e) Inversion Error Terms

Fig. 9. Spoiled Grain Position 1: Experimental imaging results of partially filled bin with hard red winter wheat at nominal 15% moisture content, containing a small region spoiled grain region (25% moisture content). Operating frequency of 78 MHz. 2D cross sectional images of the spoiled grain region. Expected permittivity of the spoiled grain target is $4.9 - j0.7$, and the background grain $3.9 - j0.38$. Expected size and location of target shown with dashed light blue line. (For interpretation of the references to colour in this figure legend, the reader is referred to the web version of this article.)

5. Results and discussion

Two sets of scattered field data were collected, with the spoilage target located at two different positions. The two sets of data were collected to ensure that any image we generated of the spoilage target would follow the target as it was moved.

5.1. Raw data analysis

To show the field probe performance, we show the $S_{x,x}$ measurements vs frequency in Fig. 7 and we show the $S_{x,y}$ measurements at 93 MHz for target position #2 in Fig. 8. The $S_{x,x}$ measurements justify our use of the term field probe instead of antennas: at the frequency range of interest, the field probes have an $S_{x,x}$ in the range of -1.5 to -3.5 dB. This means that the probes transmit, at best, approximately $1/2$ of the transceiver energy into the bin. An

antenna would normally be above 90% of the energy transmitted. However, the Fig. 8 shows that we still can obtain useful signal despite this lack of transmitter efficiency. The signal for the inversion algorithm is the scattered field measurements, and these are all well above the noise floor of the system of -120 dB.

5.2. Frequency selection

To select the imaging frequencies, we generally follow the empirical process first outlined in Gilmore et al. (2010). Our first step is to collect the incident field data with a known state (dry grain), over a wide band of frequencies. We then simulate the EM imaging system with our FEM code (Zakaria et al., 2010; Zakaria et al., 2013) and generate the expected incident fields at the receiver locations at a small number of frequencies. Next, we manually search for frequencies where the normalized magnitude
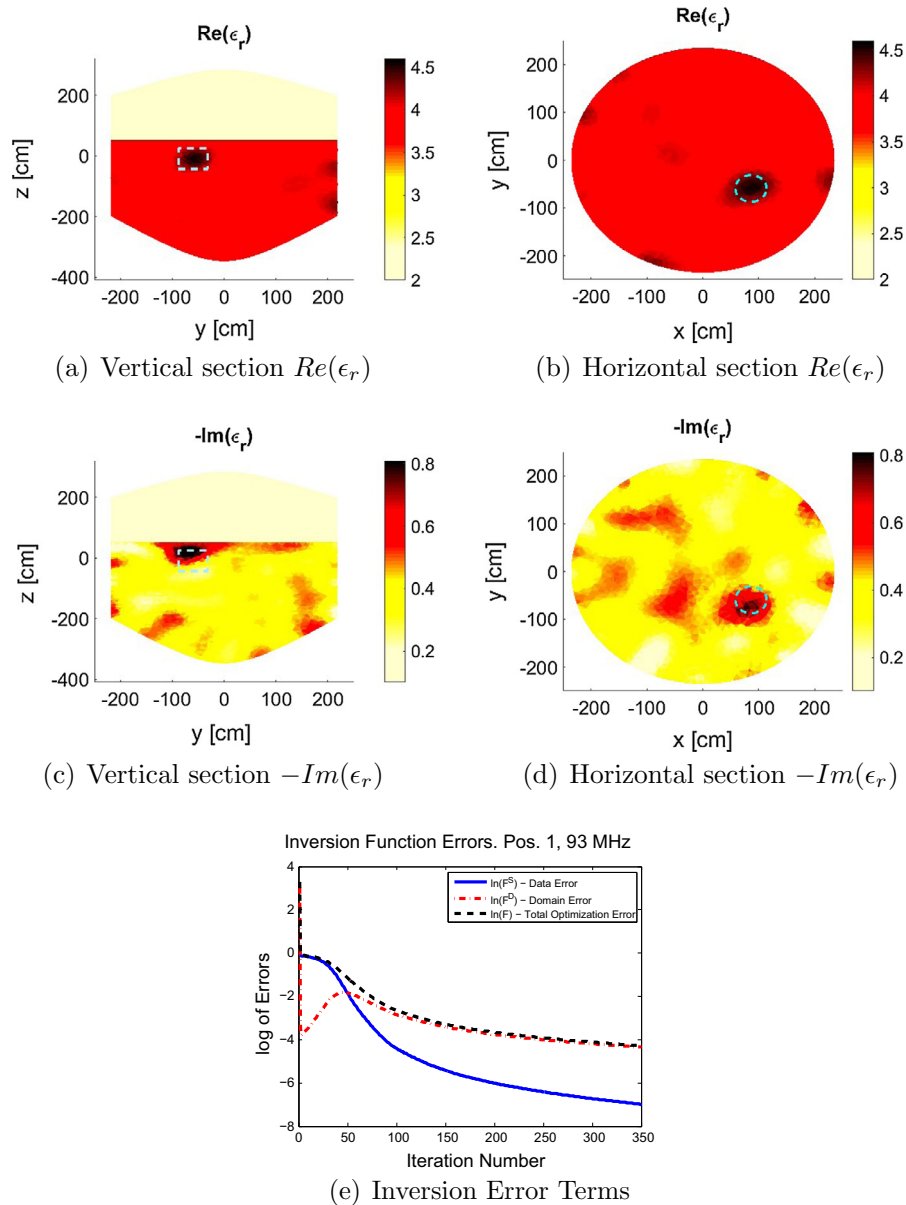

(a) Vertical section $Re(\epsilon_r)$ (b) Horizontal section $Re(\epsilon_r)$

(c) Vertical section $-Im(\epsilon_r)$ (d) Horizontal section $-Im(\epsilon_r)$

(e) Inversion Error Terms

Fig. 10. Spoiled Grain Position 1: Experimental imaging results of partially filled bin with hard red winter wheat at nominal 15% moisture content, containing a small spoiled grain region (25% moisture content). Operating frequency of 93 MHz. 2D cross sectional images of the spoiled grain region. Expected permittivity of the spoiled grain target is $4.9 - j0.7$, and the background grain $3.9 - j0.38$. Expected size and location of target shown with dashed light blue line. (For interpretation of the references to colour in this figure legend, the reader is referred to the web version of this article.)
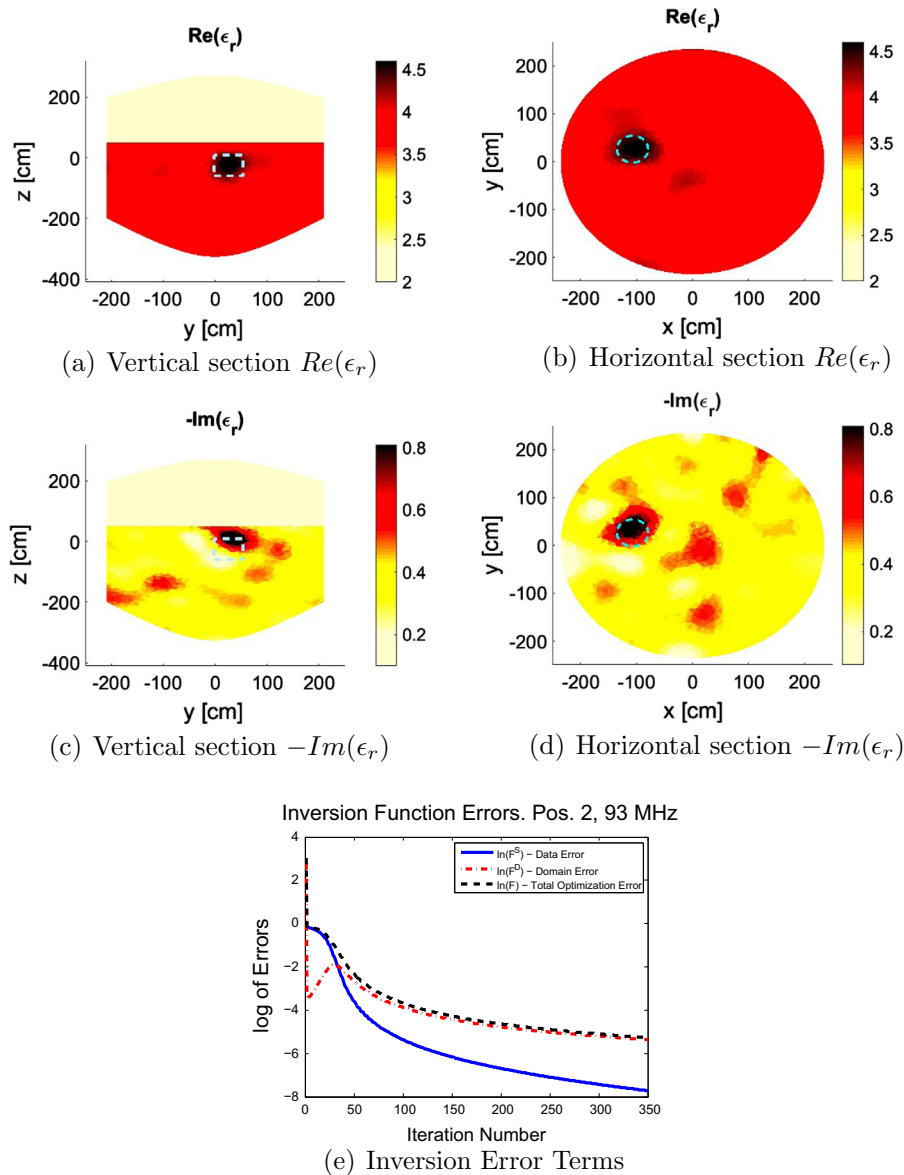
(a) Vertical section $Re(\epsilon_r)$

(b) Horizontal section $Re(\epsilon_r)$

(c) Vertical section $-Im(\epsilon_r)$

(d) Horizontal section $-Im(\epsilon_r)$

(e) Inversion Error Terms

Fig. 11. Spoiled Grain Position 2: Experimental imaging results of partially filled bin with hard red winter wheat at nominal 15% moisture content, containing a small spoiled grain region (25% moisture content). Operating frequency of 93 MHz. 2D cross sectional images of the spoiled grain region. Expected permittivity of the spoiled grain target is $4.9 - j0.7$, and the background grain $3.9 - j0.38$. Expected size and location of target shown with dashed light blue line. (For interpretation of the references to colour in this figure legend, the reader is referred to the web version of this article.)

of the experimental and simulated incident measurements are as close as possible. Our experience with EM imaging over a variety of systems has shown that this method provides frequencies where imaging is effective. This process has been developed to find the frequencies where the modeling error (the differences between the physical system and computational model) are minimized. For this system, we have found that 78 MHz and 93 MHz are two frequencies, and we show results at both of these frequencies below.

5.3. Imaging results

Two-dimensional slices of the full 3D images are shown in Figs. 9–11. In each image, the expected size and position of the spoiled grain target is shown with a light blue dotted line. For the real part of the permittivity, we have restricted the permittivty range to start at 2 (as opposed to 1). For target position #2, we have created a 3D image of $Re(\epsilon_r)$ with all solid threshold for all tetrahe-

drals with $Re(\epsilon_r) > 4.2$. This 3D image is shown in Fig. 12. For informational purposes, we have further included the optimization errors terms outlined in Eq. (5).

5.4. Discussion

Overall, the spoiled grain is clearly visible in the images. The spoiled grain clearly stands out from the background grain, and location and approximate size of the spoiled grain region is clearly indicated. This holds for both images at 78 and 93 MHz.

Further, the permittivity of the spoiled region is approximately $4.5 - j0.8$. From the real part of this value, we would predict a moisture content of approx. 21%, and from imaginary part of the permittivity we would predict a moisture content of $>25\%$ (Nelson and Stetson, 1976). Our predicted value based on 25% moisture content is $4.9 - j0.7$. We suspect that this value would be even more accurate if the spoiled grain region was larger. No matter what the exact value of the permittivity is, the fact that
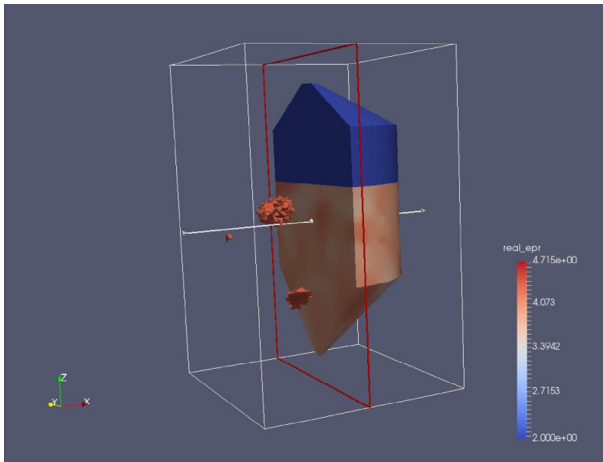
Fig. 12. 3D Spoiled Grain Position 2: Experimental imaging results of partially filled bin with hard red winter wheat at nominal 15% moisture content, containing a small spoiled grain region (25% moisture content). Operating frequency of 93 MHz. 3D image of $Re(\epsilon_r)$, with threshhold of spoilage region set to $\epsilon_r > 4.2$. Expected permittivity of the background grain $3.9 - j0.38$. The largest region of spoilage coincides with the spoiled grain target.

the spoilage region has a higher moisture content (at unsafe storage levels) is very clear.

The spoilage region is most clearly distinguished in the images of $Re(\epsilon_r)$. In the images of $Im(\epsilon_r)$, there are significant artifacts surrounding the spoiled grain. The presence of these artifacts emphasizes the importance of considering both the real and imaginary part of the permittivity: given the current state of these images, we would rely on the real part of the permittivity to detect a region of unsafe spoilage, and then use both the real and imaginary images to make an estimate of the moisture content of the spoilage region.

Our initial hypothesis regarding these artifacts was that these regions may represent actual differences in moisture content of the bulk (non-spoiled) grain, but since these artifacts change position when we re-position the spoiled grain target, they likely do not represent actual differences in moisture/temperature of grain. These spots could be unavoidable noise, or possibly interactions between modeling errors: e.g., there is a metal ladder in the bin which we do not model in our inversion code, and secondary interactions between this ladder and the scattered fields from the spoiled grain could conceivably cause artifacts of this type. The reduction of these artifacts remains a subject of future research, and there are many methods we could attempt to reduce them, including improving the signal to noise ratio of the system, building a more accurate computational model of the bin, or working on balancing methods to emphasize either the real or imaginary part of the permittivity in the reconstruction (Zakaria et al., 2012).

6. Conclusions

We have presented the first industrial-scale whole bin imaging system. This system includes field probes designed to withstand the forces of bin loading and unloading, as well as the use of literature-based estimates of the bulk-permittivity of the stored grain (as opposed to direct measurement of the permittivity). The functionality of this system was experimentally demonstrated with 55 tonnes of hard-red winter wheat in a hopper-style bin. This system was shown to be capable of detecting an artificially-introduced spoilage region of 25% moisture in a background of 15% moisture content grain, with a maximum dimension of 2/5 of a wavelength. Thus, EMI based systems for grain monitoring are industrially viable for whole-bin monitoring.

References

Abubakar, A., van den Berg, P.M., Semenov, S.Y., 2003. Two- and three-dimensional algorithms for microwave imaging and inverse scattering. J. Electromagnet. Waves Appl. 17, 209–231.

Abubakar, A., Hu, W., van den Berg, P., Habashy, T., 2008. A finite-difference contrast source inversion method. Inverse Probl. 24, 065004 (17pp).

Abubakar, A., Li, M., Pan, G., Liu, J., Habashy, T., 2011. Joint mt and csem data inversion using a multiplicative cost function approach. Geophysics 76, F203–F214.

Asefi, M., Faucher, G., LoVetri, J., 2016. Surface-current measurements as data for electromagnetic imaging within metallic enclosures. IEEE Trans. Microw. Theory Tech. 64 (11), 4039–4047.

Asefi, M., Jeffrey, I., LoVetri, J., Gilmore, C., Card, P., Paliwal, J., 2015. Grain bin monitoring via electromagnetic imaging. Comput. Electron. Agric. 119, 133–141.

Asefi, M., Zakaria, A., LoVetri, J., 2017. Microwave imaging using normal electric-field components inside metallic resonant chambers. IEEE Trans. Microw. Theory Tech. 65 (3), 923–933. http://dx.doi.org/10.1109/TMTT.2016.2627554.

Belkebir, K., Saillard, M., 2005. Testing inversion algorithms against experimental data: inhomogeneous targets. Inverse Probl. 21, S1–S3.

Di Donato, L., Bevacqua, M.T., Crocco, L., Isernia, T., 2015. Inverse scattering via virtual experiments and contrast source regularization. IEEE Trans. Antennas Propagat. 63, 1669–1677.

Dyson, J.D., 1973. Measurement of near fields of antennas and scatterers. IEEE Trans. Antennas Propagat. 21, 446–460.

FAO, 2011. Rural structures in the tropics: Design and Development. FAO. <http://www.fao.org/docrep/015/i2433e/i2433e.pdf>.

Folk, K., 2016. Intragrain. <http://intragrain.com/>.

Freeman, S.A., Kelley, K.W., Maier, D.E., Field, W.E., 1998. Review of entrapments in bulk agricultural materials at commercial grain facilities. J. Safety Res. 29, 123–134.

Gilmore, C., Mojabi, P., Zakaria, A., Ostadrahimi, M., Kaye, C., Noghanian, S., Shafai, L., Pistorius, S., LoVetri, J., 2010. A wideband microwave tomography system with a novel frequency selection procedure. IEEE Trans. Biomed. Eng. 57, 894–904. http://dx.doi.org/10.1109/TBME.2009.2036372.

Gilmore, C., Zakaria, A., Pistorius, S., LoVetri, J., 2013. Microwave imaging of human forearms: pilot study and image enhancement. J. Biomed. Imaging 2013, 19.

Hagness, S.C., Fear, E.C., Massa, A., 2012. Guest editorial: special cluster on microwave medical imaging. Antennas Wireless Propagat. Lett. IEEE 11, 1592–1597.

Haynes, M., Clarkson, S., Moghaddam, M., 2011. Electromagnetic inverse scattering algorithm and experiment using absolute source characterization. In: 2011 IEEE International Symposium on Antennas and Propagation (APSURSI), pp. 2545–2548. http://dx.doi.org/10.1109/APS.2011.599704.

Haynes, M., Stang, J., Moghaddam, M., 2012. Microwave breast imaging system prototype with integrated numerical characterization. J. Biomed. Imaging 2012, 2.

Jayas, D., Ghosh, P., Paliwal, J., Karunakaran, C., 2011. Quality evalution of wheat, pp. 351–376.

Joachimowicz, N., Pichot, C., Hugonin, J.P., 1991. Inverse scattering: an iterative numerical method for electromagnetic imaging. IEEE Trans. Antennas Propagat. 39, 1742–1753.

Kanda, M., 1993. Standard probes for electromagnetic field measurements. IEEE Trans. Antennas Propagat. 41, 1349–1364.

Kraszewski, A., Trabelsi, S., Nelson, S., 1998. Comparison of density-independent expressions for moisture content determination in wheat at microwave frequencies. J. Agric. Eng. Res. 71, 227–237.

Lawrence, K., Nelson, S., Bartley Jr, P., 1998. Measuring dielectric properties of hard redwinter wheat from 1 to 350 MHz with a flow-through coaxial sample holder. Trans. ASAE 41, 143.

Litman, A., Crocco, L., 2009. Testing inversion algorithms against experimental data: 3d targets. Inverse Probl. 25, 020201.

Maier, D., Channaiah, L., Martinez-Kawas, A., Lawrence, J., Chaves, E., Coradi, P., Fromme, G., 2010. Monitoring carbon dioxide concentration for early detection of spoilage in stored grain. Julius-Kühn-Archiv, 505.

Mallach, M., Gebhardt, P., Musch, T., 2016. 2d microwave tomography system for imaging of multiphase flows in metal pipes. Flow Measurement and Instrumentation.

Meaney, P., Fanning, M., Li, D., Poplack, S., Paulsen, K., 2000. A clinical prototype for active microwave imaging of the breast. IEEE Trans. Microwave Theory Tech. 48, 1841–1853. http://dx.doi.org/10.1109/22.883861.

Muir, W., White, N., 2000. Microorganisms in stored grain. In: Grain Preservation Biosystems, Manitoba, pp. 1–17.

Nelson, S., Stetson, L., 1976. Frequency and moisture dependence of the dielectric properties of hard red winter wheat. J. Agric. Eng. Res. 21, 181–192.

Nelson, S. et al., 2008. Dielectric properties of agricultural products and some applications. Res. Agric. Eng. 54, 104–112.

Nelson, S.O., Kraszewski, A.W., Trabelsi, S., Lawrence, K.C., 2000. Using cereal grain permittivity for sensing moisture content. IEEE Trans. Instrum. Measure. 49, 470–475.

Nelson, S.O., Trabelsi, S., 2006. Dielectric spectroscopy of wheat from 10 MHz to 1.8 GHz. Measure. Sci. Technol. 17, 2294.

Rocca, P., Benedetti, M., Donelli, M., Franceschini, D., Massa, A., 2009. Evolutionary optimization as applied to inverse scattering problems. Inverse Probl. 25, 123003.

Semenov, S., Corfield, D., 2008. Microwave tomography for brain imaging: feasibility assessment for stroke detection. Int. J. Antennas Propagat., 254830

Shea, J., Kosmas, P., Van Veen, B., Hagness, S., 2010. Contrast-enhanced microwave imaging of breast tumors: a computational study using 3d realistic numerical phantoms. Inverse Probl. 26, 074009.

Sinha, R., 1995. The Stored-grain Ecosystem. Marcel Decker Inc.

Spiegel, R.J., Booth, C.A., Bronaugh, E.L., 1983. A radiation measuring system with potential automotive under-hood application. IEEE Trans. Electromagnet. Compat., 61–69

White, N., 2000. Protection of Farm-Stored Grain, oilseeds, and Pulses from Insects, Mites and Molds.

van den Berg, P.M., Kleinman, R.E., 1997. A contrast source inversion method. Inverse Probl. 13, 1607–1620.

White, N., 2002. Safe storage guidelines.

Yang, D., Oldenburg, D.W., Haber, E., 2013. 3-d inversion of airborne electromagnetic data parallelized and accelerated by local mesh and adaptive soundings. Geophys. J. Int., ggt465

Zakaria, A., Gilmore, C., LoVetri, J., 2010. Finite-element contrast source inversion method for microwave imaging. Inverse Probl. 26, 115010.

Zakaria, A., Gilmore, C., Pistorius, S., LoVetri, J., 2012. Balanced multiplicative regularization for the contrast source inversion method. In: ACES Conference on Applied Computational Electromagnetics.

Zakaria, A., Jeffrey, I., LoVetri, J., 2013. Full-vectorial parallel finite-element contrast source inversion method. Prog. Electromagnet. Res. 142, 463–483.